Terrain-Trapped Airflows and Orographic Rainfall along the Coast of Northern California. Part I: Kinematic Characterization Using a Wind Profiling Radar

Raul A. Valenzuela[a]

Department of Atmospheric and Oceanic Sciences, and Cooperative Institute for Research in Environmental Sciences, University of Colorado Boulder, Boulder, Colorado

David E. Kingsmill

Cooperative Institute for Research in Environmental Sciences, University of Colorado Boulder, Boulder, Colorado

(Manuscript received 26 December 2016, in final form 10 April 2017)

ABSTRACT

This study develops an objective method of identifying terrain-trapped airflows (TTAs) along the coast of Northern California and documenting their impact on orographic rainfall. TTAs are defined as relatively narrow air masses that consistently flow in close proximity and approximately parallel to an orographic barrier. A 13-winter-seasons dataset is employed, including observations from a 915-MHz wind profiling radar along the coast at Bodega Bay (BBY, 15 m MSL) and surface meteorology stations at BBY and in the coastal mountains at Cazadero (CZD, 478 m MSL). A subset of rainy hours exhibits a profile with enhanced vertical shear and an easterly wind maximum in the lowest 500 m MSL, roughly the same depth as the nearby coastal terrain. Both flow features have a connection to TTAs along the coast of Northern California. Based on the average orientation (320°–140°) and altitude of nearby topography, mean wind direction in the lowest 500 m MSL ($\overline{\mathrm{WDIR}}_{500}$) between 0°–140° is used as the initial criterion to identify TTA conditions. Application of this threshold yields a CZD/BBY rainfall ratio of 1.4 (3.2) for TTA (NO TTA) conditions. More detailed analysis of the relationship between $\overline{\mathrm{WDIR}}_{500}$ and orographic rainfall reveals that an upper threshold of 150° more precisely divides the TTA and NO-TTA regimes. A sensitivity analysis and comparison with a TTA documented in a previous case study show that the best TTA identification criteria correspond to $0° \leq \overline{\mathrm{WDIR}}_{500} < 150°$ with a duration of at least 2 h. This objective identification method is applied to seven case studies in Part II of the present study.

1. Introduction

A number of studies have shown that poleward horizontal water vapor transport from the tropics to midlatitudes is mostly achieved through a narrow corridor of less than ~1000-km width and larger than ~2000-km length (e.g., Zhu and Newell 1994; Ralph et al. 2004, 2005; Bao et al. 2006). This form of water vapor transport, known as an atmospheric river (AR), is commonly found in the warm sector of extratropical cyclones and collocated with the pre-cold-frontal low-level jet (LLJ; e.g.,

Ralph et al. 2005). The west coast of the United States often experiences the landfall of these extratropical cyclones and concomitant ARs during wintertime. These storms can produce copious amounts of precipitation with a spatial distribution that is modulated by mountains (e.g., Colle et al. 2008; Hughes et al. 2009). Modulation of the background synoptic precipitation pattern due to the presence of mountains is known as orographic precipitation (e.g., Colle et al. 2013).

West Coast terrain, particularly along Northern California, is characterized by mountain peaks of ~500–1000 m MSL and steep slopes immediately adjacent to the coastline. When moist, statically neutral airflow impacts these slopes, air is generally lifted and cooled, which produces condensate and, after a finite time, precipitation-sized hydrometeors. This upslope flow mechanism is a relatively simple conceptual model that

[a] Current affiliation: Department of Geophysics, University of Chile, Santiago, Chile.

Corresponding author: Raul A. Valenzuela, raul.valenzuela@colorado.edu

can explain a significant fraction of orographic rainfall over the midlatitudes (e.g., Roe 2005; Houze 2012). However, mountains can produce their own mesoscale circulations. One example is the presence of a terrain-trapped airflow (TTA) on the windward side of orographic barriers. According to Valenzuela and Kingsmill (2015, henceforth VK15), a TTA is defined as a relatively narrow air mass consistently flowing in close proximity and approximately parallel to an orographic barrier. For example, TTAs flow poleward along the western side of coastal mountain ranges in the western United States. The study of TTAs is relevant because they can disrupt the spatial precipitation pattern normally expected when extratropical cyclones approach and make landfall over coastal terrain, potentially diminishing the forecast accuracy of flooding events that are accompanied by significant societal impacts.

Two commonly observed forcing mechanisms associated with TTAs are low-level blocking and gap flows (e.g., Smith 1979; Neiman et al. 2006; VK15). In the former, a stably stratified atmosphere facilitates the abutting of air parcels on the windward side of mountain barriers, which then turn to the left (right) in the Northern (Southern) Hemisphere as they decelerate and the along-barrier pressure gradient increases. For gap flows, a cold continental air mass exits through a mountain depression (i.e., gap) forced by an along-gap pressure gradient.

TTA impacts on orographic precipitation have been studied in association with several large-scale mountain ranges (e.g., altitudes above ~1000 m MSL) such as the European Alps (e.g., Medina et al. 2005), the Southern Alps of New Zealand (e.g., Sinclair et al. 1997), the mountainous areas of Taiwan (e.g., Yu and Hsieh 2009), Colorado's Rocky Mountains (e.g., Peterson et al. 1991), and California's Sierra Nevada (e.g., Kingsmill et al. 2013). In contrast, TTA impacts associated with small-scale mountain ranges (e.g., altitudes below ~1000 m MSL) have received much less attention. One of these relatively rare studies (Neiman et al. 2002) used wind profiler and rain gauge data along the coastal mountains of California to describe the relationship between upslope wind speed and orographic precipitation. By studying six West Coast winter storms, they found that the presence of a TTA decreased the average mountain-to-coast rainfall ratio from 5.06 to 1.26 and hypothesized that this occurred as a result of upstream lifting of the prefrontal LLJ offshore by the TTA. VK15 was another study that addressed this problem by examining ground-based scanning Doppler radar observations along and offshore of the Northern California coastal mountains during a significant landfalling winter storm to detail the three-dimensional kinematic and precipitation structure

associated with a TTA. The structures presented in their study showed that the TTA was responsible for upstream lifting of an LLJ. Furthermore, VK15 documented a precipitation enhancement zone roughly 30 km offshore and nearly parallel to the coast associated with TTA lifting of the LLJ. Both of these observations support the hypothesis offered by Neiman et al. (2002).

Although Neiman et al. (2002) and VK15 used case studies to provide some insights about the kinematic characteristics and effects of TTAs on orographic rainfall, an objective method of identifying TTA events was not developed. The former study simply relied on the average coastal terrain orientation to determine the wind direction associated with TTAs, whereas the latter considered both terrain orientation and a strong vertical shear of horizontal winds in the lowest 0.5 km MSL. The Northern California coastal terrain associated with these studies has a mean orientation of ~320°–140°, meaning that poleward-directed terrain-parallel airflow (i.e., a TTA) in this area would be characterized by a wind direction of ~140°. This wind direction would appear to be a good estimate of the threshold required to identify TTA regimes. However, no detailed evaluations of this or any other objective TTA identification scheme have been reported, a shortcoming that this investigation addresses with a long-term, 13-season dataset. This study is unique because it explores an objective method of identifying TTAs and documents the effects of TTAs on orographic rainfall using a statistically significant dataset. We hypothesize that TTAs are associated with wind directions less than or equal to 140° (i.e., from the southeast) in the lowest 500 m (average local topography altitude) and their presence reduces the mountain-to-coast rainfall ratio to near 1.

Section 2 describes the observing systems and data processing techniques employed in the analysis. A statistical characterization of low-level winds is described in section 3, while the objective identification of TTAs and documentation of their impacts on orographic rainfall is provided in section 4. Finally, section 5 presents a summary and conclusions. In the forthcoming continuation of this study (R. A. Valenzuela and D. E. Kingsmill 2017, unpublished manuscript, hereinafter Part II), the objective TTA identification method is applied to seven cases observed in detail with a ground-based X-band scanning Doppler radar to compare kinematic and precipitation structures associated with TTA and NO-TTA regimes.

2. Observing systems and data processing

Observations employed in this study were collected along the Northern California coast as part of the

California Land-Falling Jets (CALJET), Pacific Land-Falling Jets (PACJET), and Hydrometeorology Testbed experiments (Ralph et al. 2013) operated by the National Oceanic and Atmospheric Administration/Earth System Research Laboratory (NOAA/ESRL). Locations of key observing systems are shown in Fig. 1, while dates and number of hours included from each season are presented in Table 1.

The main observational asset is a 915-MHz wind profiling radar (Ecklund et al. 1988) located along the coast at Bodega Bay (BBY; 15 m MSL), which provided hourly vertical profiles of horizontal winds. Each profile was processed with the continuity method of Weber et al. (1993) that checks consistency in the dataset over time and height. Since wind profiler gate spacing and first-gate altitude vary slightly between seasons, each profile was interpolated onto a common 40-gate grid having 92-m vertical spacing with the first gate at 160 m MSL. In addition, 2′ resolution measurements of surface winds and rain accumulation were available at BBY and in the coastal mountains at Cazadero (CZD; 478 m MSL). After quality control, hourly mean winds (speed and direction) and hourly rain accumulations were derived from the native resolution observations at both sites. Hours with missing surface (BBY and CZD) or wind profiler (BBY) data were discarded, ensuring the presence of simultaneous observations.

3. Statistical characteristics of low-level winds

The impacts of LLJs and ARs on coastal orographic precipitation are normally concentrated below 3000 m MSL (e.g., Neiman et al. 2002; Ralph et al. 2004, 2005). Thus, the overall joint distribution of the wind speed and direction is now examined at selected vertical levels up to ~3000 m MSL (Fig. 2). There is a bimodal distribution at the surface (Fig. 2a), where one of the modes is associated with northwesterly flow and maximum wind speeds of 15 m s⁻¹ while the other mode is associated with easterly flow and maximum wind speeds of 9 m s⁻¹. At 160 m and 344 m MSL the wind distributions are unimodal (Figs. 2b,c), with northwesterly winds having maximum speeds of ~21 m s⁻¹. The dominant mode is still associated with northwesterly winds at 528 m MSL (Fig. 2d), but the distribution is wider, a trend that continues upward toward 2001 m MSL where the distribution becomes multimodal (Figs. 2e–j). At 2553 and 3014 m MSL the dominant mode of the wind directions is west-southwesterly (Figs. 2k,l), with maximum wind speeds up to 27 m s⁻¹.

Since this study is focused on orographic rainfall, the joint distribution of winds is now examined for the subset of data when hourly rain accumulations at CZD
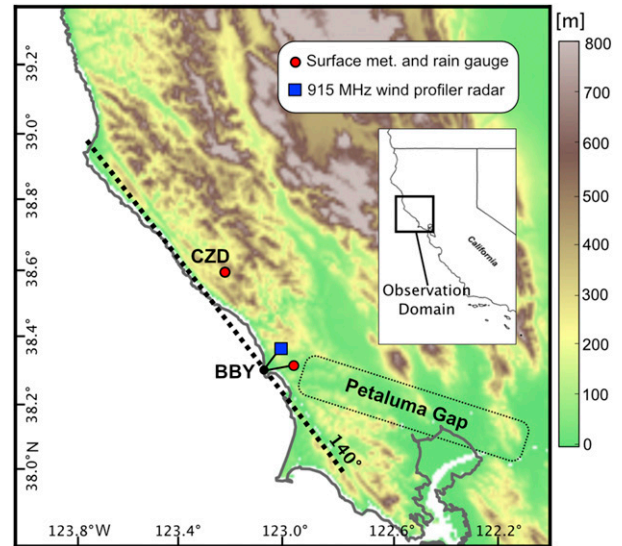

FIG. 1. Topographic map overlaid with observing systems as defined in the legend. Color scale for terrain height is to the right of the figure. Inset map shows the position of the study domain relative to the state of California. Dashed line (azimuth 140°) is a reference for the mean orientation of the coastal mountains (e.g., Neiman et al. 2002). Dotted curved rectangle indicates the location of the Petaluma Gap.

met or exceeded 0.25 mm (Table 1), the tipping-bucket gauge resolution. Wind speeds are generally higher during rainy hours compared to the overall dataset (Fig. 3). There is still a bimodal distribution of wind directions at the surface (Fig. 3a), with one of the modes associated with easterly flow. However, the other mode is now characterized by southeasterly winds. The wind distributions at 160 m and 344 m MSL are still unimodal (Figs. 3b,c), with south-southeasterly winds having maximum speeds of ~24 m s⁻¹. From 528 m MSL upward (Figs. 3d–l), wind distributions become progressively wider and show multimodal characteristics. However, the dominant modal wind direction exhibits a shift from south-southeasterly to southwesterly in rising through this layer. In addition, the frequency of winds above 24 m s⁻¹ increases from 1541 m MSL upward.

The results for the overall dataset indicate a dominance of westerly component winds, which suggests synoptic-scale forcing associated with midlatitude westerlies. In contrast, the subset of rainy hours is dominated by southerly component winds characterized by larger magnitudes, a pattern shift likely associated with approaching cyclonic and cold-frontal systems (Ralph et al. 2004; James and Houze 2005; Neiman et al. 2008).

The previous analysis highlights the modal wind distributions at discrete vertical levels. Now, to provide a more vertically continuous perspective, profiles of BBY

TABLE 1. Date and time (UTC) ranges for each of the 13 winter seasons included in the analysis. Number of hours when nonmissing rain gauge (CZD and BBY) and surface and wind profiler (BBY) observations were available simultaneously is indicated. The last column shows the number of hours for a subset of this group when hourly rain accumulation at CZD was ≥0.25 mm.

Winter season	Start time and date	End time and date	No. of observation hours	No. of observation hours when CZD rain ≥0.25 mm
1998	0000 UTC 1 Jan 1998	2300 UTC 31 Mar 1998	1839	604
2001	0000 UTC 12 Jan 2001	2000 UTC 8 Mar 2001	1153	276
2002	0200 UTC 11 Jan 2002	2300 UTC 6 Apr 2002	2062	201
2002/03	0000 UTC 9 Dec 2002	2300 UTC 9 Apr 2003	2784	458
2003/04	2200 UTC 13 Dec 2003	2300 UTC 21 Mar 2004	2378	391
2004/05	1600 UTC 12 Nov 2004	2300 UTC 1 Apr 2005	3330	487
2005/06	0000 UTC 15 Nov 2005	2300 UTC 25 Apr 2006	3145	726
2006/07	0000 UTC 1 Dec 2006	2300 UTC 30 Apr 2007	3624	428
2007/08	0000 UTC 21 Nov 2007	2300 UTC 9 Apr 2008	3384	420
2008/09	0000 UTC 8 Nov 2008	2300 UTC 11 May 2009	4440	533
2009/10	0000 UTC 6 Nov 2009	2300 UTC 11 May 2010	4233	594
2010/11	0000 UTC 2 Nov 2010	2300 UTC 31 Mar 2011	3312	533
2011/12	0000 UTC 16 Nov 2011	2300 UTC 1 May 2012	4032	430
Total			39 716	6081

mean wind speed and direction from the surface up to 3000 m MSL are shown in Fig. 4. The overall dataset displays monotonically increasing mean wind speed from $\sim 4 \, \text{m s}^{-1}$ at the surface to $\sim 14 \, \text{m s}^{-1}$ at 3000 m MSL, with speeds increasing sharply in the lowest ~ 250 m MSL (Fig. 4a). Corresponding angular mean wind directions (Weber 1991) indicate backing from 300° at the surface to 240° at 3000 m MSL (Fig. 4b). The wind speed interquartile range is about $4 \, \text{m s}^{-1}$ near the surface and $8 \, \text{m s}^{-1}$ from ~ 250 m MSL upward. The angular interquartile range indicates a near-surface variation of roughly 180° that decreases aloft to about 70°. There is a loss of good gates with altitude, especially above 1000 m MSL (Fig. 4c).

The mean wind speed profile for rainy hours shows winds of $\sim 6 \, \text{m s}^{-1}$ at the surface increasing to $\sim 17 \, \text{m s}^{-1}$ at 3000 m MSL (Fig. 4d). Corresponding mean wind directions veer from $\sim 170°$ at the surface to $\sim 230°$ at 3000 m MSL (Fig. 4e). The wind speed interquartile range is about $4 \, \text{m s}^{-1}$ near the surface and about $7 \, \text{m s}^{-1}$ through the rest of the profile except for a slightly larger variation between 250 and 1250 m MSL. The angular interquartile range indicates a near-surface variation of roughly 100° decreasing aloft to about 50°. The rainy subset has less loss of good gates with altitude relative to the overall dataset, with more than 90% of the good gates below 2000 m MSL (Fig. 4f).

Compared with the overall dataset, the rainy wind speed profile exhibits higher wind speeds and a slightly larger variation, whereas the wind direction profile reveals veering instead of backing and a significantly smaller variation. Stronger mean wind speed in the rainy hour profile is linked with the environment associated with the approaching cyclonic and cold-frontal systems

(Ralph et al. 2004; James and Houze 2005; Neiman et al. 2008). Similarly, veering winds with altitude during rainy hours suggest warm-air advection associated with the warm sector of landfalling extratropical cyclones. The larger fraction of good gates in the rainy profile is produced by an enhanced sensitivity of the wind profiler to hydrometeors at 915 MHz (e.g., Ecklund et al. 1988).

Profiles of the zonal- and meridional-component airflow provide a different but informative perspective about wind characteristics at and above BBY (Fig. 5). The mean zonal-component (U) profile for the overall dataset exhibits only positive mean velocities, with values of $\sim 1 \, \text{m s}^{-1}$ from the surface to 900 m MSL that increase monotonically upward to $8 \, \text{m s}^{-1}$ at 3000 m MSL (Fig. 5a). The zonal-component interquartile range increases from about $5 \, \text{m s}^{-1}$ in the lowest 1500 m MSL to about $10 \, \text{m s}^{-1}$ at 3000 m MSL. The mean meridional-component (V) profile shows velocities of $\sim 0 \, \text{m s}^{-1}$ below 1500 m MSL that monotonically increase upward to $4 \, \text{m s}^{-1}$ at 3000 m MSL (Fig. 5b). The meridional-component interquartile range increases from the surface to 3000 m MSL and exhibits a larger magnitude relative to the zonal component. The larger interquartile range of the meridional component might be linked to meridional perturbations associated with the passage of synoptic systems and their attendant cyclonic circulations.

Relative to the overall dataset, mean zonal-component wind speeds in the rainy-hour subset are smaller (larger) below (above) ~ 500 m MSL (Fig. 5c). The corresponding interquartile range is nearly constant with altitude and, unlike the overall dataset, indicates the presence of an easterly wind maximum of $-5 \, \text{m s}^{-1}$ below 500 m MSL. Meridional-component winds are

Wind roses at BBY for winter-season hours
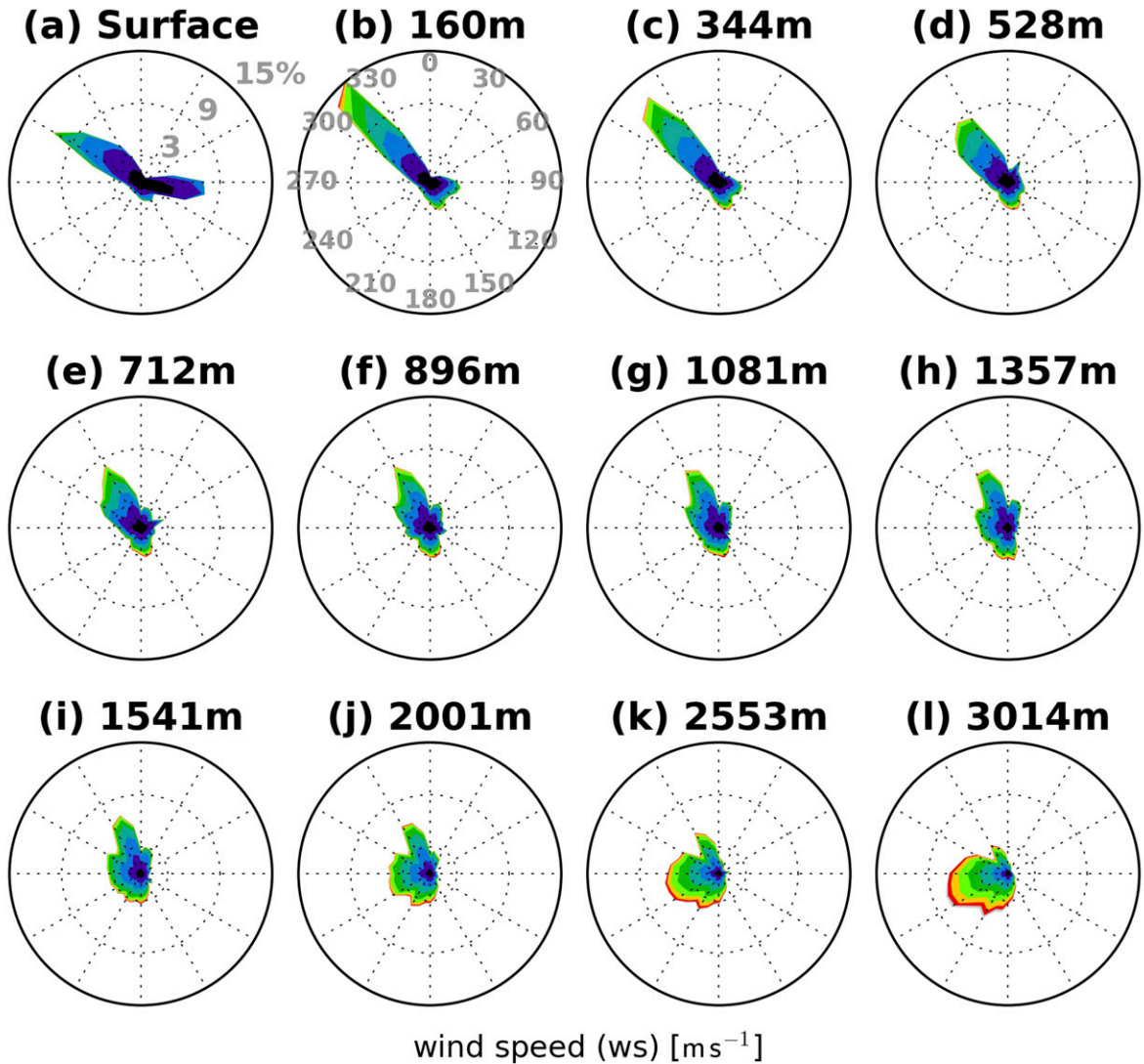
FIG. 2. BBY wind roses for the 13-winter-season dataset at (a) the surface, and at (b) 160, (c) 344, (d) 528, (e) 712, (f) 896, (g) 1081, (h) 1357, (i) 1541, (j) 2001, (k) 2553, and (l) 3014 m MSL. Wind direction (°) is indicated by the polar coordinate while frequency of occurrence (%) is indicated by the radial coordinate. Wind speeds (m s^{-1}) are represented by color shading according to the scale at bottom. Wind direction and speed bins are 10° and m s^{-1}, respectively.

significantly different relative to the overall dataset, with a dominance of southerly winds through the entire profile, most likely associated with the prefrontal environment of baroclinic wave passages (Fig. 5d). Mean meridional-component wind speeds increase sharply from ~3 to 8 m s^{-1} in the lowest 500 m MSL. Above this level, the mean values exhibit small fluctuations around 8 m s^{-1} up to 2500 m MSL and then increase slightly to 9 m s^{-1} at 3000 m MSL. The meridional-component interquartile range is relatively small near the surface but increases dramatically above ~200 m MSL, from where it holds relatively constant with altitude.
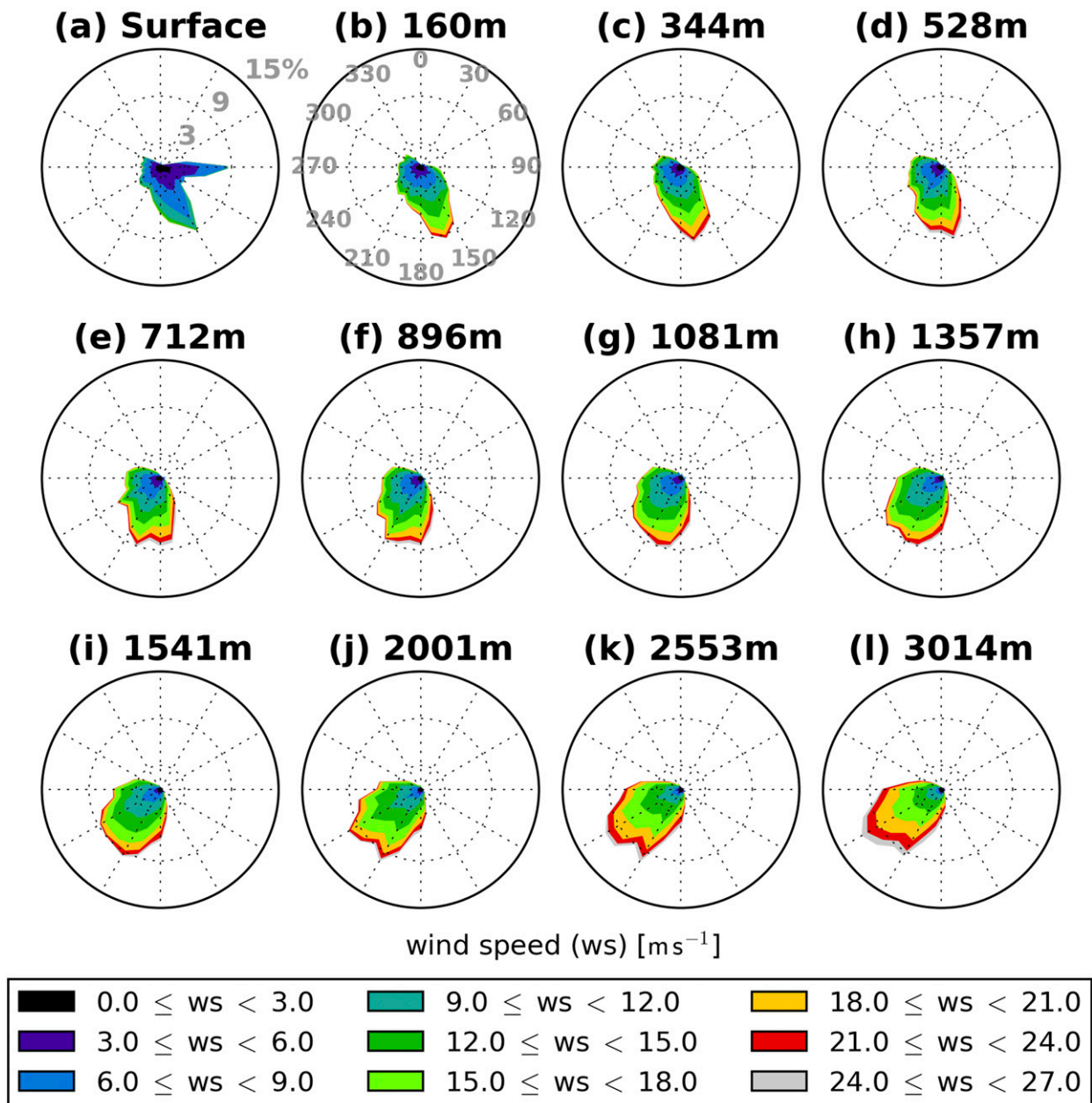
Wind roses at BBY for czd-rain hours

FIG. 3. As in Fig. 2, but for hours when rainfall ≥0.25 mm is observed at CZD.

One striking feature of the rainy subset relative to the overall dataset is the large vertical gradient of the zonal- and meridional-component winds in the lowest 500 m MSL. These structures are examined in greater detail with profiles of vertical wind shear. In the overall dataset, zonal- and meridional-component shear profiles (Figs. 6a,b) indicate mostly positive mean values with maxima of $4 \times 10^{-3} \, \mathrm{s}^{-1}$ and a homogenous variation

along the profile except for the first level. Both shear components contribute almost equally to the resulting mean vector magnitude (Fig. 6c). Note that the mean values significantly depart from the medians because of the presence of extreme values (e.g., values larger than the 95th percentile). During rainy hours, the zonal-component mean vertical shear features a maximum of $\sim 9 \times 10^{-3} \, \mathrm{s}^{-1}$ at 500 m MSL, with means around

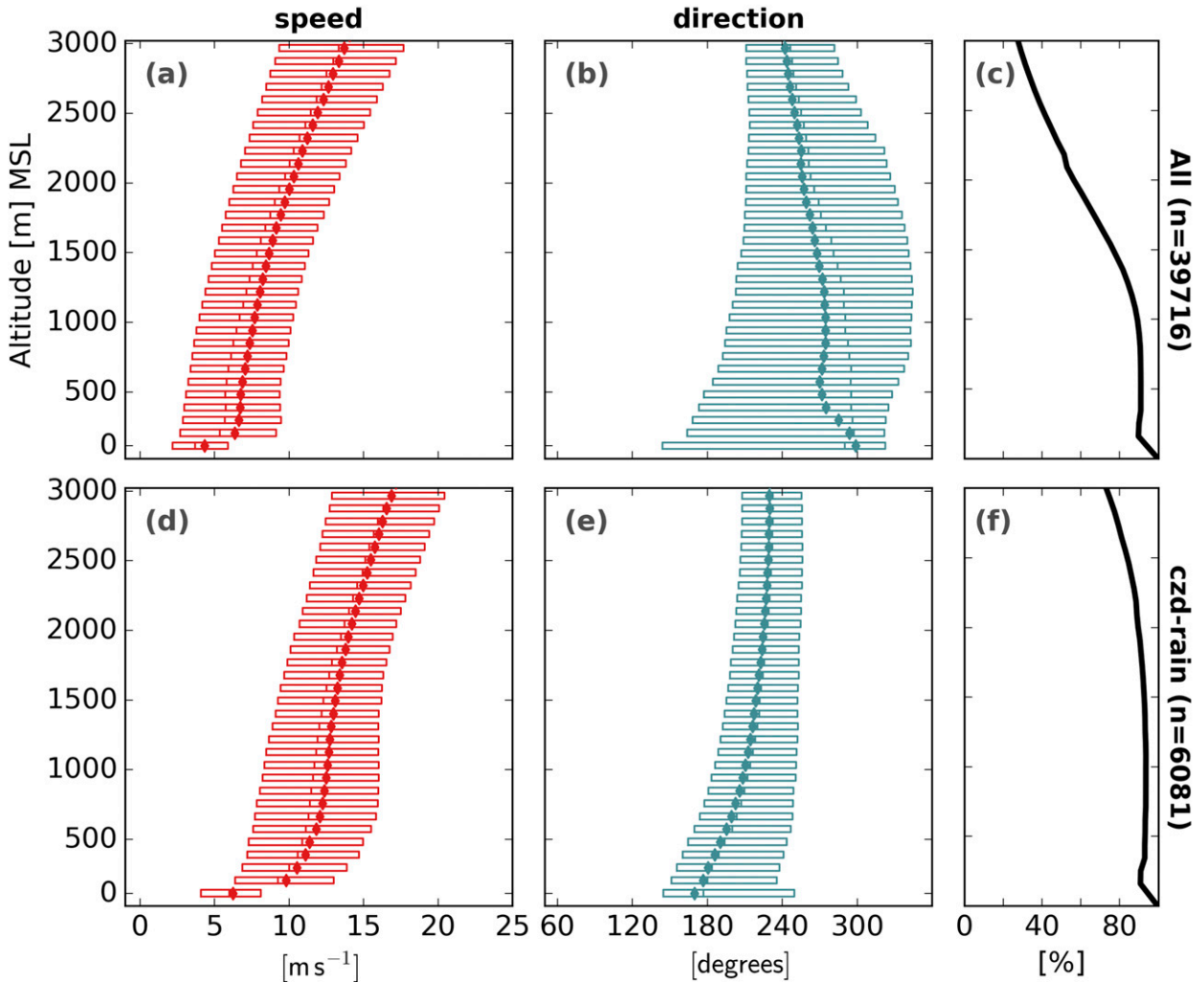## 13-season mean wind profile

FIG. 4. Profiles of BBY (a) wind speed and (b) wind direction in the lowest 3000 m MSL for the 13-winter-season dataset. Mean (median) values are indicated by the diamond marker (vertical line) along with the 25th–75th interquartile range (rectangle) at each level. (c) Relative count (%) of good data points at each vertical level. (d)–(f) As in (a)–(c), but for the subset of hours when rainfall ≥0.25 mm is observed at CZD.

$2 \times 10^{-3} s^{-1}$ near the surface and above 1000 m MSL (Fig. 6d). The meridional-component mean vertical shear (Fig. 6e) features sharply decreasing values from near the surface ($\sim17 \times 10^{-3} s^{-1}$) to ~500 m MSL and above (closer to $0 s^{-1}$). Variability increases most notably below 500 m MSL in both components. The contributions of both components result in a mean vertical wind shear vector magnitude profile with relatively large values in the lowest 500 m MSL (maximum of $29 \times 10^{-3} s^{-1}$; Fig. 6f). The mean shear vector values are closer to the medians, indicating less frequency of extreme values.

In summary, these results suggest that winds in the rainy environment have characteristics that are

distinctly different from those in the overall dataset. For example, the rainy subset is characterized by a generally southerly airflow having larger wind speeds and smaller variations in wind direction—attributes that are probably related to the predominantly meridional orientation of baroclinic wave passages. In addition, there are some wind characteristics that appear to be linked with the lowest 500 m MSL, which is approximately the same depth as the nearby coastal terrain. These characteristics include enhanced vertical wind shear (as in VK15) and conspicuous southeasterly winds [as in the blocked cases from Neiman et al. (2002)] with an easterly maximum in the zonal component wind profile, features that have a

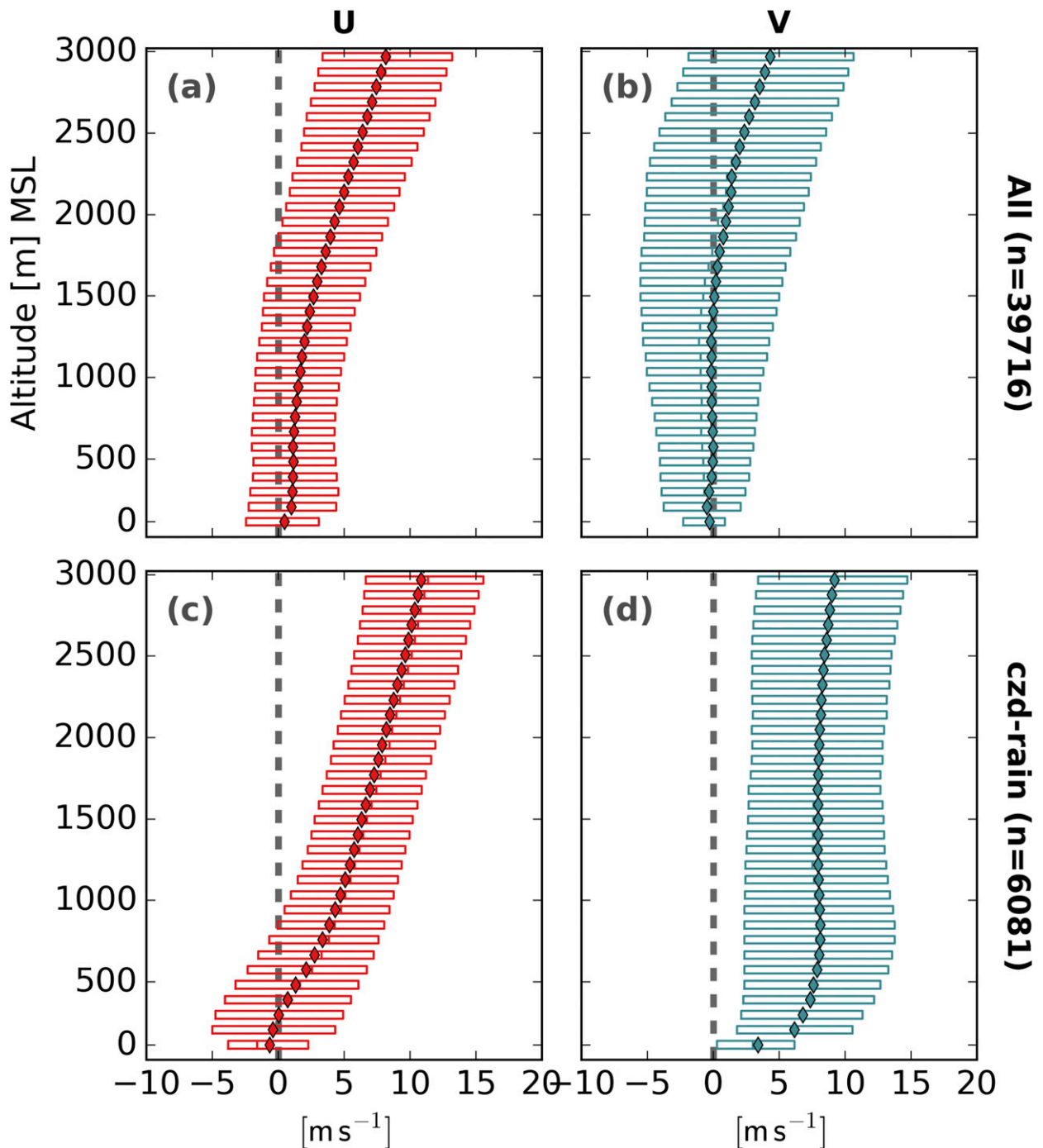# 13-season mean wind component profile

FIG. 5. Profiles of BBY (a) U (zonal) and (b) V (meridional) wind components (m s^{-1}) in the lowest 3000 m MSL for the 13-winter-season dataset. Mean (median) values are indicated by the diamond marker (vertical line) along with the 25th–75th interquartile range (rectangle) at each level. (c),(d) As in (a),(b), but for the subset of hours when rainfall $\geq$0.25 mm is observed at CZD.

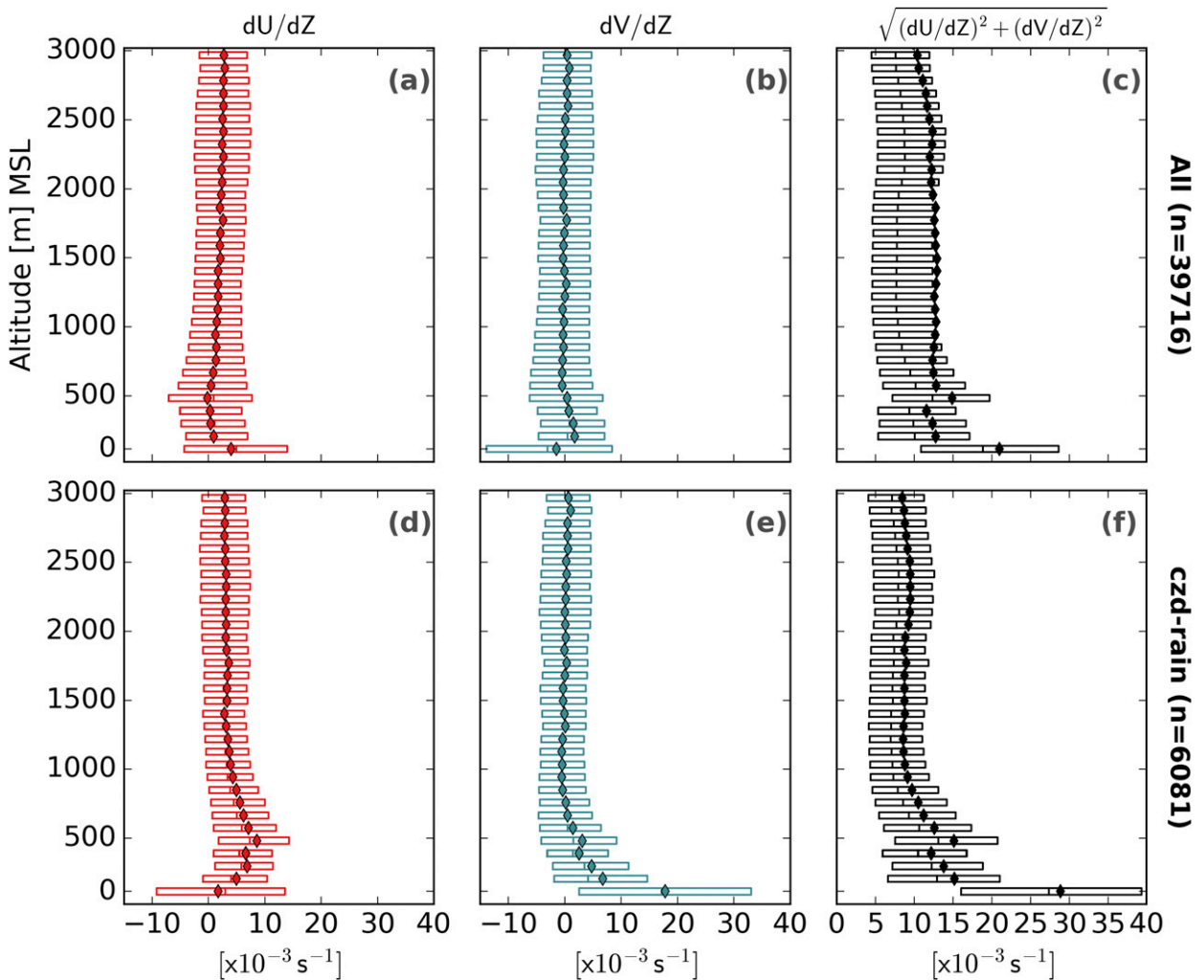## 13-season mean vertical wind-shear profile

FIG. 6. Profiles of BBY vertical shear $(10^{-3}\,s^{-1})$ for (a) U (zonal) and (b) V (meridional) component winds and (c) their vector magnitude in the lowest 3000 m MSL for the 13-winter-season dataset. Mean (median) values are indicated by the diamond marker (vertical line) along with the 25th–75th interquartile range (rectangle) at each level. (d)–(f) As in (a)–(c), but for the subset of hours when rainfall ≥ 0.25 mm is observed at CZD.

connection to TTAs along the coast of Northern California.

4. Terrain-trapped airflows

a. Objective identification

A fundamental aspect of TTAs as defined in VK15 and this study is that they are directed approximately parallel to the dominant terrain feature in their immediate vicinity. As a result, this is a reasonable criterion upon which to base an objective identification of TTAs. The coastline and coastal terrain near BBY and CZD has an average orientation of 320°–140° (Fig. 1), a

characterization that has been assumed in numerous studies (e.g., Neiman et al. 2002, 2009; Kingsmill et al. 2016). Thus, as an initial estimate, TTAs along the southwest slopes of coastal terrain in this study should be associated with wind directions of about 140°. The highest peaks and ridgeline of this terrain have an average altitude of approximately 500 m MSL. With this in mind, it is asserted that mean wind direction in the lowest 500 m MSL ($\overline{\text{WDIR}}_{500}$) should be the metric employed to objectively identify TTA conditions. Accordingly, hourly wind profiles at BBY are designated as meeting TTA conditions when $0° \leq \overline{\text{WDIR}}_{500} < 140°$. Given that wind directions between 0° and 90° are uncommon (e.g., Figs. 4b,e), this wind direction window

13-season mean wind component profile
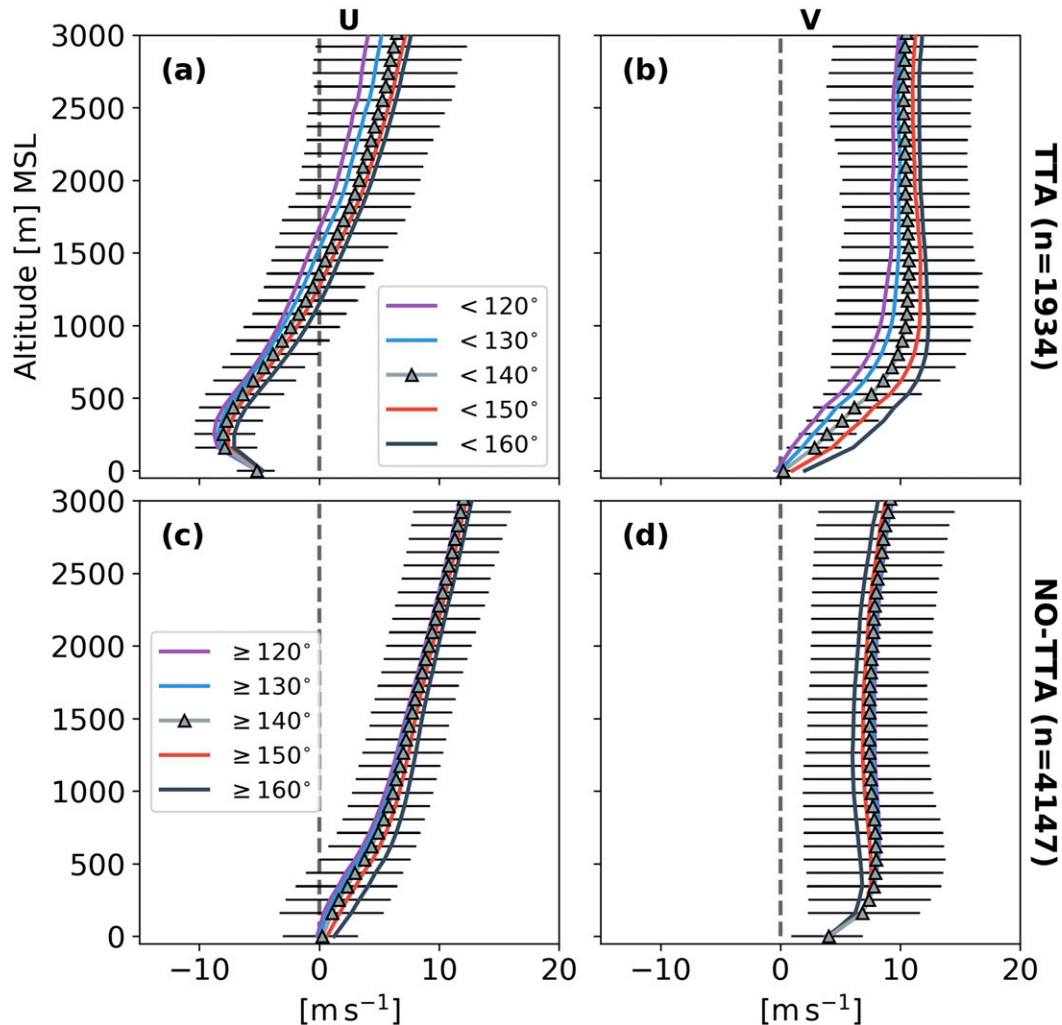## per wind direction threshold (CZD ≥ 0.25mm, n=6081)

FIG. 7. Profiles of BBY (a),(c) U (zonal) and (b),(d) V (meridional) wind components ($m\,s^{-1}$) in the lowest 3000 m MSL for the 13-winter-season dataset when rainfall ≥0.25 mm is observed at CZD. Different $\overline{WDIR}_{500}$ thresholds are employed to identify (a),(b) TTA and (c),(d) NO-TTA conditions. Legends in (a) and (c) indicate the line color associated with each threshold. Interquartile range relative to the 140° threshold is represented with horizontal lines.

can safely be used to discriminate among wind regimes associated with TTAs and allow for fluctuations in the terrain-parallel airflow direction. The NO-TTA subset is then composed of those hourly profiles with $140° \leq \overline{WDIR}_{500} < 360°$ (acknowledging that wind direction is a periodic function and $0° = 360°$). Note that a sensitivity analysis of these thresholds is discussed later in section 4c.

Zonal and meridional wind components are derived for the TTA and NO-TTA subsets. Since this study is focused on the linkage between TTAs and orographic rainfall, the analysis is applied to hours when the rain

accumulation at CZD is ≥0.25 mm. The mean zonal-component profile for the TTA regime shows easterly winds below ~1400 m MSL and westerly winds above this altitude (Fig. 7a). In addition, there is an easterly wind maximum with absolute velocity of ~8 $m\,s^{-1}$ residing below 500 m MSL and centered at ~250 m MSL. The mean meridional-component profile indicates a sharp increase of southerly winds from ~0 to 10 $m\,s^{-1}$ between the surface and 1000 m MSL, with small fluctuations of ~10 $m\,s^{-1}$ above (Fig. 7b). In contrast, the mean profile associated with the NO-TTA regime is characterized by a mean zonal-component that
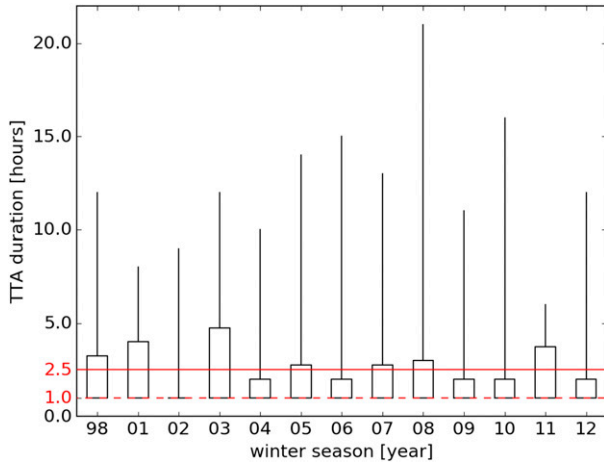
FIG. 8. Box-and-whisker plot of seasonal TTA duration distribution (h). Each box represents the 25th–75th interquartile range. Maximum TTA duration is indicated by the vertical line. Solid and dashed red lines along the horizontal axis represent the mean and median values of all seasons, respectively. Statistics are from the subset of hours when rainfall ≥0.25 mm is observed at CZD.

monotonically increases from ~1 m s^{-1} at the surface to ~12 m s^{-1} at 3000 m MSL (Fig. 7c). The corresponding meridional-component profile exhibits a more modest increase of southerly winds with altitude, fluctuating

around ~7 m s^{-1} between ~250 and 3000 m MSL (Fig. 7d). Comparing the interquartile ranges, it is evident that the TTA regime is associated with even stronger easterly winds (~−11 m s^{-1}) and smaller variability below 500 m MSL in the meridional component.

An average time scale for TTA regime occurrences during rainy conditions is derived by examining the distribution of TTA event durations in each season. Each event is defined as one or more continuous hours of TTA conditions (0° ≤ $\overline{\text{WDIR}}_{500}$ < 140°). Figure 8 shows that the seasonal distribution is significantly skewed toward 1 h, with the seasonal interquartile range varying between 1 and 4 h. Extreme values range between 6 and 21 h and the overall 13-season median and mean are 1 and 2.5 h, respectively. Since the 13-season mean represents a more complete picture of the behavior of the TTA population (i.e., it includes long-lasting TTA events), a time scale of 2.5 h seems like the most appropriate value for characterizing TTA duration.

The objective identification is applied to a storm observed on 16 February 2004, which corresponds to episode 1 in VK15. In this storm, a TTA was documented between 0900 and 1600 UTC, with an LLJ–TTA interface crossing BBY between 1500 and 1600 UTC. Figure 9a indicates that by using 0° ≤ $\overline{\text{WDIR}}_{500}$ < 140° during at least 1 h [number of hours (nh) ≥ 1], a TTA regime
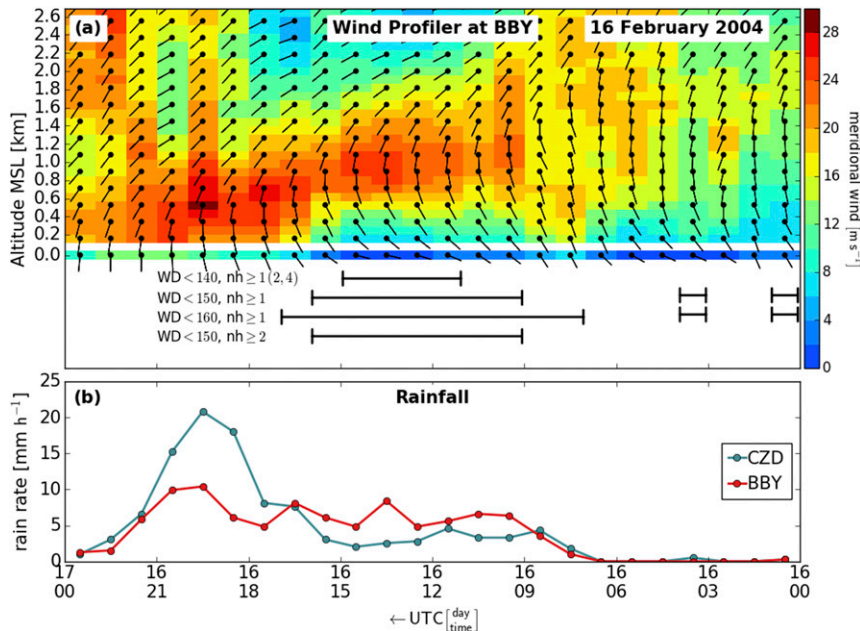

FIG. 9. (a) Time–height section of hourly surface and wind profiler observations at BBY. The V (meridional) component wind speed is shown by the colored pixels with values scaled as shown on the right. Wind staffs indicate total wind direction. Annotations at the bottom of the panel indicate TTA objective identification using different criteria. (b) Rain rate (mm h^{-1}) at BBY (red) and CZD (green) during 16 Feb 2004. In both panels, time increases from right to left to portray the advection of synoptic features from west to east.

TABLE 2. Rainfall characteristics at CZD and BBY for the 13-season dataset when hourly rain accumulations at CZD were ≥0.25 mm. In addition to the total, information is partitioned into TTA ($\overline{\text{WDIR}}_{500} < 140°$) and NO-TTA ($\overline{\text{WDIR}}_{500} < 140°$) conditions. Number of hours, rainfall accumulation (mm), relative contribution to total rainfall (%), mean rain rate (mm h^{-1}), and mountain-to-coast (i.e., CZD/BBY) rainfall ratio are indicated.

		Total	TTA	NO-TTA
Time	(h)	6081	1018	5063
CZD	(mm)	14 589	1425	13 164
	(%)	100	10	90
	(mm h^{-1})	2.4	1.4	2.6
BBY	(mm)	5068	1018	4050
	(%)	100	20	80
	(mm h^{-1})	0.8	1.0	0.8
CZD/BBY ratio		2.9	1.4	3.2

between 1100 and 1500 UTC is identified. This period is shorter than the TTA period identified in VK15 and misses the time when the LLJ–TTA interface crosses BBY. These discrepancies are discussed in section 4c.

b. Relationship to rainfall

A summary of rainfall statistics for the 13-season rainy subset (Table 2) indicates larger total accumulations at CZD (14 589 mm) compared to BBY (5068 mm), a pattern consistent with orographic enhancement as a result of an upslope forcing mechanism. The resulting mountain-to-coast (CZD/BBY) rainfall ratio is 2.9, the same as that reported by Kingsmill et al. (2016) using a similarly sized dataset but larger than the values of 2.1–2.2 observed by Neiman et al. (2002), White et al. (2003), and Neiman et al. (2009) using significantly smaller datasets. CZD and BBY rainfall accumulations associated with the TTA regime ($0° \leq \overline{\text{WDIR}}_{500} < 140°$) are 1425 and 1018 mm, respectively. The corresponding CZD/BBY ratio of 1.4 is smaller and indicative of less orographic enhancement. In contrast, NO-TTA rainfall at CZD (13 164 mm) and BBY (4050 mm) shows an orographic enhancement factor of 3.2. The TTA and NO-TTA rainfall ratio differences documented here are in agreement with VK15 and other previous studies about TTA effects on precipitation (e.g., Peterson et al. 1991; Sinclair et al. 1997; Neiman et al. 2002); namely, the presence of TTAs can produce a virtual barrier that leads to air-parcel lifting and associated precipitation development upstream of the physical barrier, reducing the precipitation gradient across the windward slope of the mountain. In Part II of this study, thermodynamic aspects of TTA forcing mechanisms (e.g., low-level blocking, gap flows) are addressed by examining seven case studies observed in the same study area.

TTA rainfall represents a slightly larger fraction of the coastal rainfall (BBY; 20%) compared to mountain rainfall (CZD; 10%). This finding is consistent with VK15's observations of precipitation enhancement offshore and along the coast in association with TTA conditions. Consequently, these results show that coastal locations are prone to receive relatively larger rainfall accumulations during TTA regimes compared to mountain sites. Rain rates are slightly larger at CZD (1.4 mm h^{-1}) compared to BBY (1.0 mm h^{-1}) during TTA conditions. However, a much more significant difference is observed during NO-TTA conditions (2.6 and 0.8 mm h^{-1}, respectively).

The partition between TTA (NO TTA) rainfall is consistent with documented decreases (increases) of orographic rainfall enhancement during TTA (NO TTA) periods (e.g., VK15; Neiman et al. 2002). Notwithstanding, the TTA period identified in the 16 February 2004 case misses a portion of time when the TTA structure was documented in VK15. As a result, the relationship between $\overline{\text{WDIR}}_{500}$ and orographic rainfall is now examined in more detail to identify any shortcomings associated with the initial criterion of a TTA regime derived with an upper threshold of 140°. Hourly rain accumulations at CZD and BBY are grouped into $\overline{\text{WDIR}}_{500}$ bins of 10° width and centered from 90° to 270° (total of 19 bins; Fig. 10). The total accumulated rainfall divided by the total number of hours in each bin produces the rain rate associated with the bin for both CZD and BBY. Confidence intervals for each rain rate were estimated with a bootstrap technique (e.g., Wilks 2011). For a given $\overline{\text{WDIR}}_{500}$ bin, this technique produces different values of accumulated rainfall as a result of a random resampling with replacement. After dividing by the number of hours (which holds the same for a given bin), the 2.5% and 97.5% percentiles are computed out of 5000 resampled rain ratios (when values converge), returning the 95% confidence interval of the rain rate. In addition to estimating the rain rate per wind direction bin, the mountain-to-coast rainfall ratio (e.g., CZD/ BBY precipitation enhancement) was computed for each wind direction bin. Rainfall ratios close to 1 indicate small or nonexistent rainfall enhancement, while values significantly greater than 1 indicate large enhancement.

Figure 10a indicates that rain rates at CZD are maximized for airflows from 180° ± 5°, while they decrease for any other direction. Although more subtle, rain rates at BBY are maximized at 140° ± 5°. The CZD/BBY rainfall ratios are relatively low (~1.5) for $\overline{\text{WDIR}}_{500}$ less than 150° while these ratios are almost twice as large for $\overline{\text{WDIR}}_{500}$ greater than 150° (Fig. 10b).

Fitting a statistical model between $\overline{\text{WDIR}}_{500}$ and the rainfall can help to clarify the mean relationship between these two variables, as well as provide an
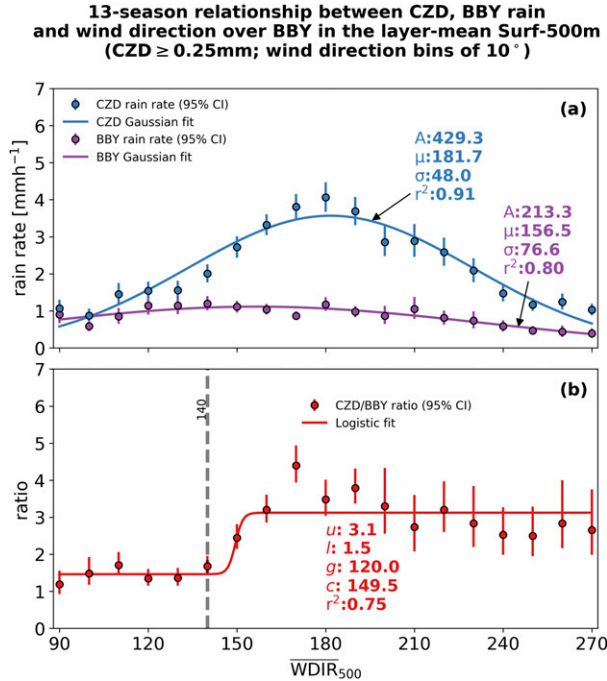
FIG. 10. (a) Relationship between rain rate (CZD and BBY) and $\overline{\mathrm{WDIR}}_{500}$ observed at BBY. Data are grouped in wind direction bins of 10° width. (b) As in (a), but for the CZD/BBY rainfall ratio. Vertical solid lines with endcaps that pass through each point correspond to 95% confidence intervals estimated with a bootstrap method. The Gaussian and logistic fits of the data are shown in (a) and (b), respectively. Vertical dashed line in (b) corresponds to the $\overline{\mathrm{WDIR}}_{500}$ value employed as the initial criterion for identifying TTA conditions.

analytical tool for future modeling studies. Two statistical models are fitted to the observed rain rates and rainfall ratios. A three-parameter Gaussian model, given by

$$f(x|\mathbf{p}) = \frac{A}{\sigma\sqrt{2\pi}} e^{-[(x-\mu)^2/(2\sigma^2)]}, \qquad (1)$$

where $\mathbf{p} \equiv (A, \mu, \sigma)$ is the parameter vector, A is the amplitude, μ is the mean, and σ is the standard deviation of the model (e.g., Larson et al. 2001), was selected for rain rates because of the bell-shaped relationship with $\overline{\mathrm{WDIR}}_{500}$. In addition, its parameter μ can be physically interpreted as the wind direction that maximizes the rain rate. A four-parameter logistic model, given by

$$f(x|\mathbf{p}) = u + \frac{l-u}{1 + (x/c)^g}, \qquad (2)$$

where $\mathbf{p} \equiv (u, l, g, c)$ is the parameter vector; u and l are the upper and lower asymptotes, respectively; g is the growth rate; and c the center of the model (e.g., Gottschalk and Dunn 2005), was selected for rainfall

ratios resulting from the sigmoidal relationship with $\overline{\mathrm{WDIR}}_{500}$. In addition, three of the logistic model parameters have physical interpretations: the upper (u) and lower (l) asymptotes represent the average rainfall enhancement in the upper and lower regimes, respectively, whereas the center c represents the wind direction where the regime changes. Parameters of each model were obtained using a least squares method.

The Gaussian fit for the CZD rain rate indicates that values are maximized for a $\overline{\mathrm{WDIR}}_{500}$ of 181.7°, whereas the BBY rain rates are maximized for $\overline{\mathrm{WDIR}}_{500}$ of 156.5° (Fig. 10a). The lower and upper regimes of the rainfall-ratio logistic fit have average ratios of 1.5 and 3.1, respectively, and the change in rainfall ratio regime occurs at 149.5° (Fig. 10b). All of these models provide a reasonable fit to the observations, with coefficients of determination (r^2) of 0.91, 0.80, and 0.75, respectively. Fitted parameters and associated coefficients of determination do not change significantly when $\overline{\mathrm{WDIR}}_{500}$ bins of 30° width are employed (not shown).

c. Sensitivity analysis

Since the relationship between $\overline{\mathrm{WDIR}}_{500}$ and rainfall indicates that an upper threshold of 150° more precisely divides TTA and NO-TTA regimes, the initial threshold of 140° is now reexamined within the context of a threshold sensitivity analysis. In addition to 140° and 150°, $\overline{\mathrm{WDIR}}_{500}$ thresholds of 120°, 130°, and 160° are employed to provide a more complete sensitivity test. There are not significant structural differences in TTA zonal-component profiles for the various thresholds (Fig. 7a). Not surprisingly, smaller-valued thresholds are associated with smaller-valued zonal-component flow (stronger easterly flow). Threshold variations in the TTA meridional component indicate that larger thresholds are associated with not only stronger southerly winds but also larger vertical shear in the lowest 1000 m MSL (Fig. 7b). Profiles of the zonal- and meridional-component flow for the NO-TTA regime are relatively insensitive to the choice of $\overline{\mathrm{WDIR}}_{500}$ threshold (Figs. 7c,d).

The sensitivity analysis is further quantified by computing the TTA and NO-TTA rainfall partitions for different thresholds of $\overline{\mathrm{WDIR}}_{500}$, durations, and layer-mean depths. Table 3 shows that the initial $\overline{\mathrm{WDIR}}_{500}$ threshold of 140° produces nearly the same CZD/BBY rainfall ratio for both TTA and NO-TTA conditions regardless of the duration threshold. Not surprisingly, longer-duration thresholds result in a smaller number of TTA hours. With a constant duration threshold of 1 h and varying $\overline{\mathrm{WDIR}}_{500}$ thresholds, CZD/BBY rainfall ratios in association with TTA conditions increase modestly for $\overline{\mathrm{WDIR}}_{500}$ greater than 140°. A similar trend is not observed for NO-TTA conditions. As $\overline{\mathrm{WDIR}}_{500}$

TABLE 3. Sensitivity analysis of layer depth, duration, and layer-mean wind direction thresholds used to identify TTA conditions. Resulting variations in rain rate (mm h^{-1}) at CZD and BBY, mountain-to-coast (i.e., CZD/BBY) rainfall ratio, and duration (h) of TTA and NO-TTA conditions are indicated.

			TTA				NO-TTA			
Layer (m)	Hours ≥	WDIR$_{Layer}$ <	CZD (mm h^{-1})	BBY (mm h^{-1})	CZD/BBY rainfall ratio	Duration (h)	CZD (mm h^{-1})	BBY (mm h^{-1})	CZD/BBY rainfall ratio	Duration (h)
0–500	1	140°	1.4	1.0	1.4	1018	2.6	0.8	3.2	5063
0–500	2	140°	1.5	1.1	1.4	783	2.5	0.8	3.1	5298
0–500	4	140°	1.6	1.2	1.3	579	2.5	0.8	3.1	5502
0–500	8	140°	1.6	1.2	1.3	301	2.4	0.8	3.0	5780
0–500	1	120°	1.2	0.8	1.5	571	2.5	0.9	2.8	5510
0–500	1	130°	1.3	0.9	1.4	759	2.5	0.8	3.1	5322
0–500	1	150°	1.7	1.0	1.7	1399	2.6	0.8	3.2	4682
0–500	1	160°	2.0	1.0	2.0	1934	2.5	0.8	3.1	4147
0–1000	1	140°	1.2	0.8	1.5	502	2.5	0.9	2.8	5579
0–500	2	150°	1.8	1.2	1.5	1118	2.5	0.8	3.1	4963

increases, the total number of TTA hours decreases. Finally, employing a 0–1000-m MSL layer-mean wind direction threshold ($\overline{\text{WDIR}}_{1000}$) of 140° with a 1-h duration threshold yields CZD/BBY rainfall ratios that are comparable to those for a 0–500-m MSL layer mean in TTA conditions (1.5 vs 1.4) but slightly smaller than those for a 0–500-m MSL layer in NO-TTA conditions (2.8 vs 3.2).

Sensitivity parameters discussed in Table 3 are now applied to identify TTA periods for the 16 February 2014 storm (Fig. 9a). A $\overline{\text{WDIR}}_{500}$ threshold of 140° and a duration threshold of 4 h (nh ≥ 4) produces the same result as nh ≥ 1 since the TTA period for $\overline{\text{WDIR}}_{500}$ < 140° is 4 h. $\overline{\text{WDIR}}_{500}$ < 150° and nh ≥ 1 produces a TTA period more consistent with the VK15 results but also includes TTA identifications for single hours beginning at 0000 and 0300 UTC. Although these hours fit the criteria imposed, the rain rates at CZD and BBY during these periods (Fig. 9b) indicate that only a minimal amount of rainfall was observed, so TTA effects on orographic rainfall can be neglected. A $\overline{\text{WDIR}}_{500}$ threshold of 160° and duration threshold of 1 h identifies a TTA period longer than 0900–1600 UTC (VK15), including times of the NO-TTA regime before 0900 and after 1600 UTC. As with the 150° threshold, there are isolated hours beginning at 0000 and 0300 UTC that can be ignored because of a lack of rainfall.

5. Summary and conclusions

This study has developed an objective identification of terrain-trapped airflows (TTAs) along the coast of Northern California and documented their impacts on orographic rainfall with a long-term, 13-season dataset. Observations from a 915-MHz wind profiling radar along the coast at BBY and surface meteorology stations

at BBY and in the coastal mountains at CZD were the main sources of data employed in this investigation.

The overall 13-winter-season dataset indicated a high frequency of northwesterly and westerly flows in the lowest ~3000 m MSL; however, winds shifted to a predominantly southerly and southwesterly component after restricting the dataset to those hours when rain accumulation at CZD is ≥0.25 mm. In addition, the rainy subset was associated with stronger wind speeds and wind directions that veer with height, a signature likely related to the presence of warm sectors embedded in extratropical cyclones making landfall over the observing domain. Notably, the rainy-subset winds exhibited enhanced vertical shear and an easterly wind maximum in the lowest 500 m MSL (Figs. 5c,d and 6d–f), which is approximately the same depth as the nearby coastal terrain. Both of these features have a connection to TTAs.

Based on the average orientation and altitude of topography near BBY and CZD, the mean wind direction in the lowest 500 m MSL (0° ≤ $\overline{\text{WDIR}}_{500}$ < 140°) was used as the initial criterion for identifying TTA conditions. Employing this threshold revealed a distinct easterly wind maximum structure of zonal-component winds at ~250 m MSL and enhanced meridional-component winds, especially above 500 m MSL (Figs. 7a,b). The TTA regime duration varied seasonally, with a mean 13-season duration of 2.5 h.

The portion of the rainy subset coupled with TTA conditions produced a CZD/BBY (i.e., mountain to coast) rainfall ratio of 1.4 while the portion coupled with NO-TTA conditions produced a ratio of 3.2. Moreover, it was found that TTA conditions were associated with a relatively large contribution to rainfall at BBY (20%) compared to CZD (10%), which is consistent with the results of VK15. However, utilization of the $\overline{\text{WDIR}}_{500}$ upper threshold of 140° produced some inconsistencies

relative to the TTA documented in VK15. A more detailed analysis of the relationship between $\overline{WDIR}_{500}$ and orographic rainfall revealed that an upper threshold of 150° more precisely divides two regimes of orographic enhancement (Fig. 10b): one with a CZD/BBY rainfall ratio of 1.5 (TTA regime) and the other with 3.1 (NO-TTA regime).

A sensitivity analysis using different TTA thresholds for layer-mean wind directions, durations, and layer-mean depths indicated that $0° \leq \overline{WDIR}_{500} < 150°$ produces results more consistent with those of VK15. However, this approach yielded some hours with negligible rainfall. Adding a TTA duration requirement of at least 2 h (i.e., nh ≥ 2) filtered out these isolated data points (Fig. 9a) and retrieved a period when the precipitation gradient across the windward slope of the mountain is reduced (Fig. 9b), a documented effect of TTAs on orographic precipitation. As a result, it is asserted that the joint thresholds of $0° \leq \overline{WDIR}_{500} < 150°$ and nh ≥ 2 produce the best objective TTA identification for orographic precipitation events.

This investigation of TTAs was associated with extratropical cyclones migrating eastward and impacting the nearly two-dimensional coastal mountains of Northern California. It is unclear whether the TTA identification approach developed for this locale will be applicable to other geographic settings with potentially different topographic and synoptic-forcing characteristics. Future studies should address this issue.

Part II of this study incorporates the aforementioned TTA identification criteria (i.e., $0° \leq \overline{WDIR}_{500} < 150°$ and nh ≥ 2) to isolate TTA periods in seven case studies and produce composited TTA kinematic and precipitation structures using a ground-based scanning Doppler radar located at a coastal site north of BBY. In addition, Part II will include a theoretical analysis of TTA forcing.

REFERENCES

Bao, J. W., S. A. Michelson, P. J. Neiman, F. M. Ralph, and J. M. Wilczak, 2006: Interpretation of enhanced integrated water vapor bands associated with extratropical cyclones: Their formation and connection to tropical moisture. *Mon. Wea. Rev.*, **134**, 1063–1080, doi:10.1175/MWR3123.1.

Colle, B. A., Y. Lin, S. Medina, and B. F. Smull, 2008: Orographic modification of convection and flow kinematics by the Oregon Coast Range and Cascades during IMPROVE-2. *Mon. Wea. Rev.*, **136**, 3894–3916, doi:10.1175/2008MWR2369.1.

——, R. B. Smith, and D. A. Wesley, 2013: Theory, observations, and predictions of orographic precipitation. *Mountain Weather Research and Forecasting*, F. K. Chow, S. F. J. D. Wekker, and B. J. Snyder, Eds., Springer Atmospheric Sciences, Springer, 291–344, doi:10.1007/978-94-007-4098-3_6.

Ecklund, W. L., D. A. Carter, and B. B. Balsley, 1988: A UHF wind profiler for the boundary layer: Brief description and initial results. *J. Atmos. Oceanic Technol.*, **5**, 432–441, doi:10.1175/1520-0426(1988)005<0432:AUWPFT>2.0.CO;2.

Gottschalk, P. G., and J. R. Dunn, 2005: The five-parameter logistic: A characterization and comparison with the four-parameter logistic. *Anal. Biochem.*, **343**, 54–65, doi:10.1016/j.ab.2005.04.035.

Houze, R. A., Jr., 2012: Orographic effects on precipitating clouds. *Rev. Geophys.*, **50**, RG1001, doi:10.1029/2011RG000365.

Hughes, M., A. Hall, and R. G. Fovell, 2009: Blocking in areas of complex topography, and its influence on rainfall distribution. *J. Atmos. Sci.*, **66**, 508–518, doi:10.1175/2008JAS2689.1.

James, C. N., and R. A. Houze Jr., 2005: Modification of precipitation by coastal orography in storms crossing northern California. *Mon. Wea. Rev.*, **133**, 3110–3131, doi:10.1175/MWR3019.1.

Kingsmill, D. E., P. J. Neiman, B. J. Moore, M. Hughes, S. E. Yuter, and F. M. Ralph, 2013: Kinematic and thermodynamic structures of Sierra barrier jets and overrunning atmospheric rivers during a landfalling winter storm in northern California. *Mon. Wea. Rev.*, **141**, 2015–2036, doi:10.1175/MWR-D-12-00277.1.

——, P. O. G. Persson, S. Haimov, and M. D. Shupe, 2016: Mountain waves and orographic precipitation in a northern Colorado winter storm. *Quart. J. Roy. Meteor. Soc.*, **142**, 836–853, doi:10.1002/qj.2685.

Larson, V. E., R. Wood, P. R. Field, J.-C. Golaz, T. H. V. Haar, and W. R. Cotton, 2001: Small-scale and mesoscale variability of scalars in cloudy boundary layers: One-dimensional probability density functions. *J. Atmos. Sci.*, **58**, 1978–1994, doi:10.1175/1520-0469(2001)058<1978:SSAMVO>2.0.CO;2.

Medina, S., B. F. Smull, R. A. Houze Jr., and M. Steiner, 2005: Cross-barrier flow during orographic precipitation events: Results from MAP and IMPROVE. *J. Atmos. Sci.*, **62**, 3580–3598, doi:10.1175/JAS3554.1.

Neiman, P. J., F. M. Ralph, A. B. White, D. E. Kingsmill, and P. O. G. Persson, 2002: The statistical relationship between upslope flow and rainfall in California's coastal mountains: Observations during CALJET. *Mon. Wea. Rev.*, **130**, 1468–1492, doi:10.1175/1520-0493(2002)130<1468:TSRBUF>2.0.CO;2.

——, ——, ——, D. D. Parrish, J. S. Holloway, and D. L. Bartels, 2006: A multiwinter analysis of channeled flow through a prominent gap along the northern California coast during CALJET and PACJET. *Mon. Wea. Rev.*, **134**, 1815–1841, doi:10.1175/MWR3148.1.

——, ——, G. A. Wick, J. D. Lundquist, and M. D. Dettinger, 2008: Meteorological characteristics and overland precipitation impacts of atmospheric rivers affecting the west coast of North America based on eight years of SSM/I satellite observations. *J. Hydrometeor.*, **9**, 22–47, doi:10.1175/2007JHM855.1.

——, A. B. White, F. M. Ralph, D. J. Gottas, and S. I. Gutman, 2009: A water vapour flux tool for precipitation forecasting. *Water Manage.*, **162**, 83–94, doi:10.1680/wama.2009.162.2.83.

Peterson, T. C., L. O. Grant, W. R. Cotton, and D. C. Rogers, 1991: The effect of decoupled low-level flow on winter orographic clouds and precipitation in the Yampa River valley. *J. Appl. Meteor.*, **30**, 368–386, doi:10.1175/1520-0450(1991)030<0368:TEODLL>2.0.CO;2.

Ralph, F. M., P. J. Neiman, and G. A. Wick, 2004: Satellite and CALJET aircraft observations of atmospheric rivers over the eastern North Pacific Ocean during the winter of 1997/98. *Mon. Wea. Rev.*, **132**, 1721–1745, doi:10.1175/1520-0493(2004)132<1721:SACAOO>2.0.CO;2.

——, ——, and R. Rotunno, 2005: Dropsonde observations in low-level jets over the northeastern Pacific Ocean from CALJET-1998 and PACJET-2001: Mean vertical-profile and atmospheric-river characteristics. *Mon. Wea. Rev.*, **133**, 889–910, doi:10.1175/MWR2896.1.

——, and Coauthors, 2013: The emergence of weather-related test beds linking research and forecasting operations. *Bull. Amer. Meteor. Soc.*, **94**, 1187–1211, doi:10.1175/BAMS-D-12-00080.1.

Roe, G. H., 2005: Orographic precipitation. *Annu. Rev. Earth Planet. Sci.*, **33**, 645–671, doi:10.1146/annurev.earth.33.092203.122541.

Sinclair, M. R., D. S. Wratt, R. D. Henderson, and W. R. Gray, 1997: Factors affecting the distribution and spillover of precipitation in the Southern Alps of New Zealand—A case study. *J. Appl. Meteor.*, **36**, 428–442, doi:10.1175/1520-0450(1997)036<0428:FATDAS>2.0.CO;2.

Smith, R., 1979: The influence of mountains on the atmosphere. *Advances in Geophysics*, Vol. 21, Academic Press, 87–230.

Valenzuela, R. A., and D. E. Kingsmill, 2015: Orographic precipitation forcing along the coast of northern California during a landfalling winter storm. *Mon. Wea. Rev.*, **143**, 3570–3590, doi:10.1175/MWR-D-14-00365.1.

Weber, B. L., D. B. Wuertz, D. C. Welsh, and R. McPeek, 1993: Quality controls for profiler measurements of winds and RASS temperatures. *J. Atmos. Oceanic Technol.*, **10**, doi:10.1175/1520-0426(1993)010<0452:QCFPMO>2.0.CO;2.

Weber, R., 1991: Estimator for the standard deviation of wind direction based on moments of the Cartesian components. *J. Appl. Meteor.*, **30**, 1341–1353, doi:10.1175/1520-0450(1991)030<1341:EFTSDO>2.0.CO;2.

White, A. B., P. J. Neiman, F. M. Ralph, D. E. Kingsmill, and P. O. G. Persson, 2003: Coastal orographic rainfall processes observed by radar during the California Land-Falling Jets experiment. *J. Hydrometeor.*, **4**, 264–282, doi:10.1175/1525-7541(2003)4<264:CORPOB>2.0.CO;2.

Wilks, D. S., 2011: *Statistical Methods in the Atmospheric Sciences*. 3rd ed. Elsevier, 676 pp.

Yu, C.-K., and Y.-H. Hsieh, 2009: Formation of the convective lines off the mountainous coast of southeastern Taiwan: A case study of 3 January 2004. *Mon. Wea. Rev.*, **137**, 3072–3091, doi:10.1175/2009MWR2867.1.

Zhu, Y., and R. E. Newell, 1994: Atmospheric rivers and bombs. *Geophys. Res. Lett.*, **21**, 1999–2002, doi:10.1029/94GL01710.